A fast MOSFET rf switch for low-field NMR and MRI

Pierre-Jean Nacher, Sashika Kumaragamage, Geneviève Tastevin, Christopher P. Bidinosti

THE UNIVERSITY OF WINNIPEG Laboratoire Kastler Brossel Physique quantique et applications
Published in *J. Magn. Reson.* 310 (2020) 106638, with corrections (May 31, 2022)

A fast MOSFET rf switch for low-field NMR and MRI

Pierre-Jean Nacher*[1], Sashika Kumaragamage[2,3], Geneviève Tastevin[1], and Christopher P. Bidinosti†[4,3]

[1] *Laboratoire Kastler Brossel, ENS-Université PSL, CNRS, Sorbonne Université, Collège de France; 24 rue Lhomond, 75005 Paris, France.*
[2] *Rady Faculty of Health Sciences, College of Medicine, University of Manitoba, Winnipeg, MB R3T 2N2, Canada.*
[3] *Department of Physics and Astronomy, University of Manitoba, Winnipeg, MB R3T 2N2 Canada.*
[4] *Department of Physics, University of Winnipeg, Winnipeg, MB R3B 2E9 Canada.*

Abstract TRansmit Array Spatial Encoding (TRASE) MRI uses trains of rf pulses alternatively produced by distinct transmit coils. Commonly used coil switching involving PIN diodes is too slow for low- and ultra-low-field MRI and would introduce wait times between pulses typically as long as each individual pulse in a few mT. A MOSFET-based rf switch is described and characterised. Up to hundreds of kHz, it allows for sub-μs switching of rf currents from a single amplifier to several coils with sufficient isolation ratio and negligible delay between pulses. Additionally, current switching at null current and maximum voltage can be used to abruptly stop or start pulses in series-tuned rf coils, therefore avoiding the rise and fall times associated with the Q-factors. RF energy can be efficiently stored in tuning capacitors for times as long as several seconds. Besides TRASE MRI, this energy storage approach may find applications in fast repeated spin-echo experiments. Here, a three-fold acceleration of TRASE phase-encoding is demonstrated when MOSFET switches are used instead of fast reed relays.

Keywords: Low-field NMR; low-field MRI; ultra-low-field MRI; MOSFET switch; TRASE; phase-gradient rf coils

1 Introduction

Motivation for this work comes from our interest in potential low- and ultra-low-field uses of a new NMR imaging technique known as transmit array spatial encoding (TRASE) [1, 2]. With this method, spatial encoding is achieved through the application of phase gradients of the resonant radiofrequency (rf) field – rather than magnitude gradients of the static field – and in general requires as many as two distinct phase-gradient coils per encoding direction. Moreover, traversal through k-space with TRASE requires a rapid train of π-pulses alternately generated by such phase-gradient coils. As a result, fast switching between multiple transmit coils, via single or multiple rf amplifiers [3, 4], is imperative for efficient TRASE imaging.

Positive-intrinsic-negative (PIN) diodes have proven to make effective switches for rf frequencies in the MHz range [5], but are unsuitable for the much lower frequencies (< 150 kHz) that we have been exploring [6, 7, 8, 9]. This results from the fact that rf filters or bias-T schemes are used for the PIN-diode bias control, which prevents switching times from being shorter than at least several rf periods. Mechanical contact switching, using eletromagnetically actuated reed relays (which can operate in a low-field environment) or electrostatically actuated micro electro-mechanical switches (MEMS, which can also be used in high-field conditions) introduces significant switching times, with associated limitations in achievable TRASE imaging capabilities.

Power metal oxide semiconductor field effect transistors (MOSFETs) are off-the-shelf devices available with a wide range of electrical characteristics. In regard to this work, their ability to withstand high applied voltages and flowing currents [10] make them appropriate for low-frequency rf switching. We have developed a set of MOSFET-based switches to distribute large rf currents to several transmit coils, and report here on their characterisation and efficiency for the management of rf pulses involved in TRASE imaging. With their sub-μs switching times and their wide bandwidth (down to DC currents), they can be used to switch currents in static field or gradient coils as well, and applications to signal duplexing [11] and low-frequency Q-switching [12] have been reported.

The structure of this article is the following: In Sec. 2 we describe prototype MOSFET-based switches and the different rf transmit coils used for the TRASE imaging tests. Section 3 describes electrical characterisations of the switches for three kinds of loads: resistive, inductive (an untuned transmit coil), and resonant (a series-tuned transmit coil). Potential uses for rf pulse shaping are introduced. Section 4 is devoted to the demonstration of rf switching operation for series of TRASE phase-encoding jumps in k-space in different directions. A comparison of performance of the MOSFET switches with the previously used reed relay switches is performed. The significant acceleration (up to 3-fold in this comparison) of k-space travel is finally discussed in Sec. 5.

*nacher@lkb.ens.fr, corresponding author.
†c.bidinosti@uwinnipeg.ca.

2 Hardware description

2.1 Switch circuit schematic

Figure 1a displays the circuit schematic of our bidirectional (AC) rf switch, with optically isolated and independently floating gate control. Two MOSFETs (Q_A and Q_B)

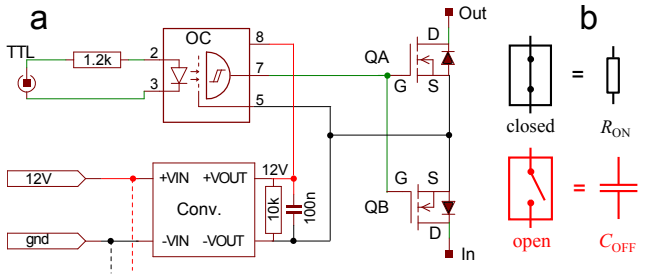

Figure 1: Electronic circuit diagram of one AC switch (a) and simplified equivalent circuits in the open and closed states (b). A single 12-V supply is used to power all switches which are fully floating and isolated from each other. Conv: DC-DC converter (Traco TMA 1212S in this prototype); OC: Optocoupler (Avago HPCL 2201); QA,QB: Power MOSFETs (see Tab. 1).

in a back-to-back configuration with connected sources are used as a standard solution to avoid the bypass of a single MOSFET in the OFF-state by its drain-source body diode during the half-cycles when $V_D < V_S$. With this design, the open and closed states of each switch are expected to be well described by the equivalent schematics of Fig. 1b.

Prototypes comprising three elementary switches (see Fig. 1 and Ref. [13]) were wired on 77.5×10 cm^2 PCBs encased in shielding boxes. Each MOSFET was fitted with a 25-mm-long heat sink (thermal resistance: 18 °K/W). The most relevant characteristics of the three MOSFETS actually tested in the prototype switches are listed in Table 1.

	V_{DS}^{max} (V)	I_D (A)	$I_{D,pulse}$ (A)	R_{DS} (Ω)	$C_{DS}^{(10)}$ (pF)	$C_{DS}^{(30)}$ (pF)
IRF540	100	28	110	0.05	500	250
IRF840	500	8	32	0.85	600	200
SCT2H12	1700	3.7	9	1.15	60	35

Table 1: Main electrical characteristics of three tested MOSFETs from the datasheets of the manufacturers (Vishay Siliconix for the IRFs and ROHM for the high-voltage SiC SCT2H12). All switching times are stated to be shorter than 100 ns. V_{DS}^{max}: maximum drain-source voltage; I_D or $I_{D,pulse}$: maximum continuous or pulsed drain currents; R_{DS}: drain-source on-state resistance; $C_{DS}^{(10)}$ and $C_{DS}^{(30)}$: examples of off-state output capacitance at V_{DS} = 10 V and 30 V, respectively. C_{DS} values depend on drain-source voltage, and one should consult the datasheets if considering, for example, low-V_{DS} values that would be relevant for noise isolation in the open state between rf pulses (i.e., during signal acquisition) or for signal distortions during zero-crossings.

2.2 RF transmit coils

It is useful at this point to describe the various rf transmit coils used in this work. Drawings of the coils are shown in Fig. 2; their naming scheme and a brief description of their design follows here. The uniform coil (U) comprises

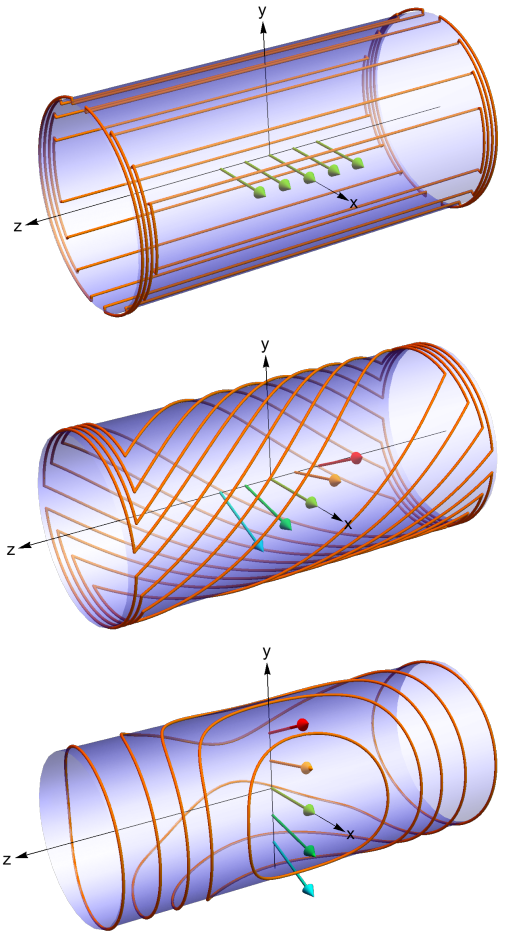

Figure 2: Wire drawings of the U (top), PG_Z (middle) and PG_Y (bottom) rf coils. All coils were wound with 0.43 mm diameter copper wire on poly(methyl methacrylate) (a.k.a. PMMA or acrylic) tubes of length 290 mm, with outer diameters of 150 mm, 133 mm, 120 mm, respectively. The arrows highlight the nominal field distributions in the central region of each coil, with spatial phase distinguished by color to guide the eye.

four saddle-coil elements, whose current arcs and number of turns were determined by numerical optimisation of field homogeneity. The resulting azimuthal angles locating the axial current rungs (in the first quadrant) are 19.1°, 39.2°, 59.8°, and 82.0°, and the numbers of turns on the corresponding saddle-coil element are 2, 4, 6, and 6. A smaller version of this coil (smU), with 1/3 the radius and the same length, was built to the same specifications for MR experiments on samples smaller than reported in this work. Here it was used only for electrical characterisation. The z phase-gradient coil (PG_Z) comprises four saddle-coil elements, each of 5 turns, that are twisted by

a 180° angle over their length. The azimuthal half-angles subtending the spiral rungs are 29.0°, 51.3°, 67.8°, and 82.8°, which come from the line current approximation to the sine-phi surface current distribution (see Eq. (D.7) of Ref. [14]). As such, the PG_Z coil is the wire-wound analog of a spiral birdcage design [15]. Finally, the y phase-gradient coil (PG_Y) comprises six current elements, each of 5 turns, that were determined using a target field design method [6, 16].

Figure 2 also shows the nominal field distributions associated with each rf coil type. These are all linear coils that generate oscillating, as opposed to rotating, rf fields. Ignoring the trivial temporal dependence, then, the nominal fields for the U, PG_Z, and PG_Y coils can be written, respectively, in the following forms:

$$\boldsymbol{B}_{\mathrm{rf}} = B_{\mathrm{rf}}\,\hat{\boldsymbol{x}} \tag{1}$$

$$\boldsymbol{B}_{\mathrm{rf}}(z) = B_{\mathrm{rf}}\left(\cos(gz)\hat{\boldsymbol{x}} + \sin(gz)\,\hat{\boldsymbol{y}}\right), \tag{2}$$

$$\boldsymbol{B}_{\mathrm{rf}}(y) = B_{\mathrm{rf}}\left(\cos(gy)\,\hat{\boldsymbol{x}} + \sin(gy)\hat{\boldsymbol{y}}\right). \tag{3}$$

The constant g is the phase gradient. For a uniform coil, $g = 0$. By twisting the PG_Z coil in the opposite direction, one would reverse the sign of its phase gradient. For the PG_Y coil, this is achieved by rotating the entire structure by 180° about the z-axis. Rotations of ±90° about the z-axis would produce x phase-gradient coils (PG_X).

As mentioned earlier, k-space traversal with TRASE requires multiple rf coils. More specifically, each coil must have a distinct phase-gradient vector $\boldsymbol{g}$ such that the spatial phase of its rf field ($\boldsymbol{g}\cdot\boldsymbol{r}$) is a unique function of position $\boldsymbol{r}$. As a result, spatial encoding with TRASE can be achieved with coils that have a different sign, magnitude and/or direction of $\boldsymbol{g}$. Here, for example, we use the U and PG_Z coils to encode along the z-direction, and the U and PG_Y coils to encode along the y-direction. More sophisticated schema for multi-dimensional encoding are discussed in Refs. [1, 2]. The phase-gradient vectors and other parameters of our coils are summarised in Table 2.

Coil	R (Ω)	L (μH)	Q	$\boldsymbol{g}$ (°/cm)
smU	2.2	60	–	0
U	5.0	350	15	0
PG_Z	6.0	380	16	7.0 $\hat{\boldsymbol{z}}$
PG_Y	2.6	120	8	6.1 $\hat{\boldsymbol{y}}$

Table 2: RF coil parameters: DC resistance R, inductance L, quality factor Q at $f = 83.682$ kHz, and nominal phase-gradient vector $\boldsymbol{g}$. The latter was computed via the Biot-Savart law for PG_Z and PG_Y along the respective axis indicated in Fig. 2.

3 Electrical characterisations

The electrical characteristics of prototype switches were assessed for the MOSFETs listed in Table 1 using three kinds of loads: resistive, inductive (an untuned transmit coil), and resonant series-tuned coils. All tests were performed using the same in-house rf power amplifier, comprising a complementary bipolar transistor pair in a class AB output stage and a driving OPA552 high-voltage (±30 V) operational amplifier. The rf pulses fed to the amplifier and the TTL control of the switches were managed by an Apollo Tecmag console (low-frequency LF1 model). Currents were inferred from voltages across a non-inductive 1-Ω resistor inserted in the ground return line at the output of the amplifier. Signals were recorded using a 4-channel digital oscilloscope (Tektronix DPO2014).

3.1 Resistive load

For these experiments the switches were located near the amplifier which was connected to their common input via a 30-cm-long coaxial cable. This strongly reduced the current across the capacitance of this connection which would be observed for an ideal open switch. The output of one switch was connected to a 50-Ω non-inductive load, as schematically displayed in Fig. 3a. Recordings were performed at frequencies f ranging from 27 to 250 kHz, between our lowest operating NMR frequency and the upper bandwidth limit of our rf amplifier. Figure 3 displays the changes in current for the MOSFETs having the largest (Fig. 3b) and smallest (Fig. 3c) output capacitances. The frequency $f_0 = 83.682$ kHz used for these recordings corresponds to a rf period $\tau_0 = 1/f_0$ of almost exactly 11.95 μs. Given that our console has a 0.1-μs time base for sequence events this makes programming complex rf sequences a simpler task than for arbitrary frequencies for which a more elaborate bookkeeping of delays would be needed. After the switch was turned off, at $t = 0$ in the recordings, the currents could be linked with the admittances $2\pi f C_{\mathrm{OFF}}$ of the switches in the open state (see Fig. 1b). They were found to vary linearly with f, as expected for currents through a capacitor, and C_{OFF} values of order 400 pF and 20 pF for the open switch were inferred for these MOSFETs, in fair agreement with the datasheet values (Table 1).

3.2 Inductive load

Tests of the response of an untuned, low-inductance coil (smU in Table 2) were performed for rectangular rf pulses applied through one switch, with switch control synchronous with pulse gating. As expected, the measured current was observed to depend strongly on the start phase φ_{s} of the rf voltage V_{rf} at the beginning of the pulse at time $t = t_{\mathrm{s}}$:

$$V_{\mathrm{rf}}(t) = V_{\mathrm{m}}\cos\left[2\pi f_0\,(t - t_{\mathrm{s}}) + \varphi_{\mathrm{s}}\right]. \tag{4}$$

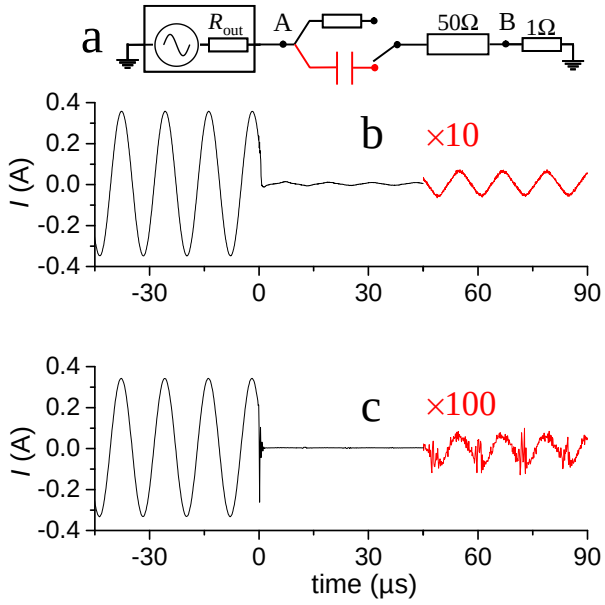

Figure 3: Current recordings at frequency f_0 through the switch of Fig. 1 using a 50 Ω load (the equivalent open and closed states of Fig. 1b are displayed). A 41-Vpp output voltage of the amplifier was used (monitored at point A in the schematic diagram a) and current was inferred from voltage at point B. Traces b and c were obtained with IRF840 and SCT2H12 MOSFETs, respectively. The rf pulse ended and the switch was opened (turned off) at time $t = 0$. The vertical scales are expanded for $t > 45$ μs to more clearly display the strongly attenuated currents.

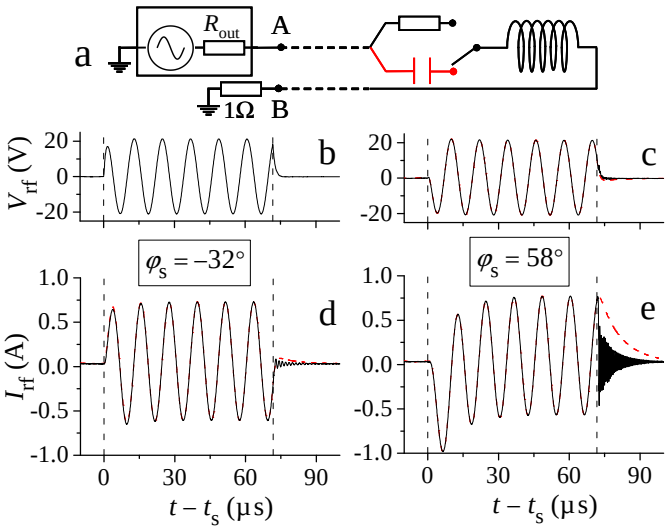

Figure 4: Voltage (at point A, panels b and c) and current (d and e) recordings at frequency f_0 through the switch (with IRF840 MOSFETs) in the untuned smU coil (circuit diagram a). Voltage pulses with magnitude $V_m = 22$ V, duration 6 τ_0, and start phases φ_s (see legends) were used. The vertical dashed lines indicate the start and stop of the rf pulses sent to the amplifier and of the switch gating. The red dashed traces in d and e are recordings for rf pulses through a permanently closed switch. Panel d corresponds to the usually desired operational mode and panel e to a worst-case scenario.

Figure 4 displays examples of voltage and current recordings for two values of the start phase when a pulse lasting an integer number of rf periods was applied (the start and end phase of V_{rf} at the beginning and end of the pulse were then equal). In these and all subsequent experiments, the switch was connected to the rf amplifier via a 4-m-long coaxial cable of capacitance $C_{conn} \approx 400$ pF (the dashed connections in Fig. 4a). The current bypassing the switch and coil load was independently assessed and suitable corrections were used to infer the currents $I_{rf}(t)$ actually flowing in the coil from voltages $V_B(t)$ recorded at point B: $I_{rf}(t) = V_B(t)/R_{1\Omega} - C_{conn} dV_{rf}(t)/dt$.

The start phase of V_{rf} in Fig. 4b was chosen to obtain a near-sine current response (Fig. 4d). Step-like initial and final voltage jumps were prevented by the finite slew-rate of the rf amplifier. Since the reactive part of the coil impedance, $2\pi f_0 L \approx 32$ Ω, was significantly larger than the total resistive component R_{tot} of the circuit (of the coil, switch, and internal impedance of the amplifier), the current response in the coil was significantly phase-shifted:

$$I_{rf}(t) = I_m \cos\left[2\pi f_0 (t - t_s) + \phi_s\right], \qquad (5)$$

with a start phase $\phi_s = \varphi_s - 80°$. Using the standard phase shift expression $\tan(\phi_s - \varphi_s) = 2\pi f_0 L/R_{tot}$, the value $R_{tot} = 5.6$ Ω is inferred.

For a start phase of V_{rf} in quadrature with the previous setting (Figs. 4c and 4e) the initial current response exhibits a large offset which decays with a time constant of order 10 μs consistent with the value of L/R_{tot}. At the end of the voltage pulse, if the switch remained closed (red dashed line in Fig. 4e), the current decayed to zero with the same time constant, but when the switch was turned off at the end of the pulse (black solid line in Fig. 4e) the decaying DC current was blocked and a high-frequency ($f_{hf} = 1.7$ MHz) decaying current was observed. This corresponds to the damped oscillation of a series LCR circuit with a capacitance value of 150 pF for $L = 60$ μH, also consistent with the datasheet value for C_{OFF} albeit lower than inferred from the resistive load measurements.

Note that a high-frequency damped current oscillation induces a high oscillating voltage across both the coil and the open switch (not shown here). Its typical magnitude is larger than the driving rf voltage V_m during the pulse by a factor of order f_{hf}/f_0 (20 in this case). This barely remained within the maximum voltage capability of the selected MOSFET components in this test. With their much smaller C_{OFF} value, and the potentially higher f_{hf} value (depending on coil self-resonance and wiring details), the SCT2H12 MOSFETs would be more easily damaged by current switching in an inductive load unless care is taken to switch at zero-current-crossing times. They were therefore not tested in this configuration.

3.3 Resonant (series-tuned) load

The response of the series-tuned U coil (see Table 2) to rectangular rf voltage pulses driven through the switch was characterised for resonant rf (Fig. 5a). The first in

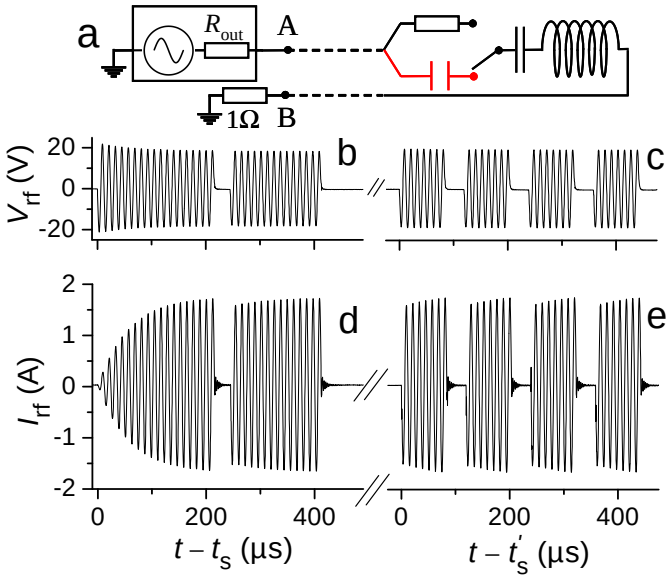

Figure 5: Voltage (panels b and c) and current (d and e) recordings at frequency f_0 in the tuned U coil (circuit diagram a). The switch (with IRF840 MOSFETs) was closed only during the rectangular rf pulses. b,d: a pair of 18- and 14-τ_0-long voltage pulses with magnitude $V_m = 20$ V was used. The gap between the pulses was 2.5-τ_0 long and the phase of the rf carrier was 180°-shifted for the second pulse, yielding the same start phase $\varphi_s = 90°$. c,e: a series of 7-τ_0-long voltage pulses with the same magnitude and start phase was applied, with 3-τ_0-long delays between pulses. The difference $t_s' - t_s$ was 1061-τ_0-long ($\approx$ 12.8 ms) in this example. Energy built up during the first "charging" pulse was efficiently stored in the tuning capacitor between pulses, and more than 90% was recovered every time the switch was closed again with a suitable timing (see text).

a series of pulses (voltage in Fig. 5b, current in Fig. 5d) strongly differed from the corresponding response of an untuned coil (Figs. 4b and 4d): the current magnitude increased to approach its asymptotic value with a rate γ_I while the voltage magnitude at point A decreased with increasing current due to the voltage drop in the output impedance R_{out} of the amplifier. The quality-factor $Q = \pi f_0/\gamma_I$ inferred from the energy build-up rate $\gamma_I/2$ is indeed the same as was obtained from resonance linewidths (the time constant $1/\gamma_I$ is 4.7 τ_0 in Fig. 5d, hence $Q = 15$, as in Table 1). $R_{out} = 2.2\ \Omega$ is inferred from fits to the voltage and current data, using model functions similar to Eqs. 4 and 5, with exponentially time-dependent magnitudes $V_m(t)$ and $I_m(t)$ and additional constant offsets. Current and voltage had equal phases, and when the first pulse was interrupted and the switch opened after 18 τ_0 the phases were equal to the voltage start phase.

The second pulse in Figs. 5b and 5d was obtained by closing the switch and applying rf with a start phase in that pulse equal to the phase at the end of the previous pulse. This was achieved by combining a delay of a half-integer number of periods and a 180° phase shift of the pulse carrier wave. The current oscillations immediately resumed from a large magnitude which approached again its asymptotic value. Here we chose the magnitudes and durations of this pair of pulses to induce a 2π rotation followed by a -2π rotation of magnetisation for H nuclei in a water sample (see Sec. 4.2). This choice was made to prepare a suitably charged tuning capacitor and induce a negligible loss of magnetisation in the sample (this scheme aiming at preserving the initial magnetisation is robust with respect to rf field inhomogeneity or amplitude changes).

The four subsequent pulses in Figs. 5c and 5e were obtained by closing the switch and applying rf once again taking care to resume current oscillation with the suitable start phase in each pulse. Here, it was achieved by using the same carrier phase for all pulses and integer numbers of periods for the delay difference $\Delta t = t_s' - t_s$, the pulse durations, and the inter-pulse gaps. The same fraction of the pulse magnitude was lost by each switching action and recovered during each pulse: repeated pulses yielded identical actions on magnetisation in a sample, namely π rotations in this case.

In all cases displayed in Fig. 5, the same small fraction (9.3±0.2%) of the current magnitude at the end of each pulse was lost when the next pulse was resumed. A loss fraction $\kappa = C_{OFF}/(C + C_{OFF})$ can be attributed to the operation of the switch: each time it was opened, this fraction of the charge was rapidly transferred to the switch, leaving a fraction $1-\kappa$ of the charge and voltage across the tuning capacitor after a brief transient oscillation. With $C_{OFF} \approx 400$ pF (see Sec. 3.1) and $C = 10.3$ nF (for the U coil), $\kappa \approx 4\%$ is expected. The remainder of the loss is so far unexplained, but the overall distortion of pulse shapes is small, and the practical consequences on pulse sequence design can be easily managed.

To study energy storage in the switch over longer time scales, we ran complementary experiments varying the delay Δt between the initial pulse pair and the subsequent pulses up to 10^6 τ_0 ($\approx$ 12 s). When the switch was simply closed with null rf magnitude instead of the series of applied pulses, ringdown of the stored energy (at frequency f_0) occurred from an initial current with a constant magnitude 9.5% lower than that at the end of the second pulse for $\Delta t \leq 1.2$ s, and an additional loss of 0.9% was found for $\Delta t = 12$ s. However, when rf excitation was resumed as in Figs. 5c and 5e, phase slips of 4° and 40° and correspondingly enhanced losses were observed for $\Delta t = 1.2$ s and 12 s, respectively. These losses did not result from a loss of charge in the tuning capacitor, thanks to negligible current leak in the capacitor and the switch, but from the relative difference (10^{-7}) between the exact value of $1/f_0$ and the (very good) approximation used for the rf periods in the timings of the sequences.

4 Application to accelerating TRASE imaging

This section reports on the comparison of operation and performance of the MOSFET switches and of previously used electromechanical relay switches in 1D TRASE phase encoding. The experimental setup used in combination with the switches and rf transmit coils of Sec. 2 is briefly outlined, and the MR sequences used to test k-space travel are described. Results are finally shown and discussed.

4.1 Additional experimental elements

The experiments were performed using a home-made low-field MRI system similar to the one described in Ref [17] with, however, new coil systems for improved performance. The static field was produced by a set of five coaxial circular coils with horizontal z-axis wound on PET-P (Ertalyte) formers (29 cm outer diameter, 30 cm total length). With a total power dissipation of 11 W/mT^2, no forced cooling of the coils was needed for operation up to 2.5 mT. Three sets of gradient imaging coils were used for first-order field shimming as well as for applying gradient pulses. Experiments were performed inside a 0.5-mm thick copper Faraday cage reducing interference noise at the operating frequency f_0 [18].

With the U, PG$_Z$, and PG$_Y$ transmit coils nested inside the system, a 3×8.5×8.5 cm^3 PMMA cell was installed inside the resulting 11-cm bore. Its internal 1×7×7 cm^3 volume was filled with doped water (2.8 mM $CuSO_4$, yielding $T_1 \approx T_2 \approx$180 ms). It was centred in the system and oriented in the vertical yz-plane (see the axes orientations in Fig. 2). A 75-mm-long receive coil (330 turns in 3 layers of 0.5-mm-diameter enamelled Cu wire) was wound on the 80×20 mm^2 rectangular section surrounding the water sample. With a 3.4 mH inductance, it was tuned to f_0 with a parallel capacitor ($Q = 37$) and used for NMR detection. With this crossed-coil orientation, inductive coupling to the transmit coils could be minimised. Further reduction of saturation of the detection and of distortion of the $\boldsymbol{B}_{\mathrm{rf}}$ field map was achieved using a normally-closed electromechanical relay to disconnect the coil from its tuning capacitor during rf pulses. Electronic feedback was used to decrease the Q-factor (to $Q = 8$) in order to actively broaden the detection bandwidth and accelerate saturation recovery without noise penalty [19].

In addition to generating rf excitation pulses, the LF1 Apollo Tecmag console was used for data acquisition through a high-impedance, low-noise preamplifier (SR560, Stanford Research Systems) and to manage preamplifier blanking and relay control (through HCPL-2231 optocouplers located inside the Faraday cage). The console gradient control unit and an in-house gradient amplifier were used to manage the imaging and spoiling gradients as defined in the measurement sequences.

The data obtained using the MOSFET switches were compared to those obtained using reed relays (MEDER DIP05-2A72-21L) used in prior TRASE studies for transmit coil switching [9]. They have a nominal operate time of 0.5 ms, but switching could be accelerated by driving the relays by SN7406 open-collector buffers. A 15V supply was used with a 200-Ω resistor in series with each relay actuating coil. The measured switching times were 70 μs (first contact) – 150 μs (end of bouncing) to close and less than 20 μs to open. The rated life expectancy is 10^8-10^9 cycles, typically corresponding to 10^2 to 10^4 TRASE images, but we found that the actual lifetime was reduced about tenfold, possibly because they were used to carry currents larger than their 1.25A rated capability.

4.2 k-travel sequences

Two sequences have been used to evaluate the action of TRASE phase-encoding using two of the transmit coils (U and PG$_Z$ or U and PG$_Y$) and fast MOSFET switches or slower relay switches. The corresponding fast and slower sequences have similar global structures, schematically represented in Fig. 6a. The core of each sequence is a

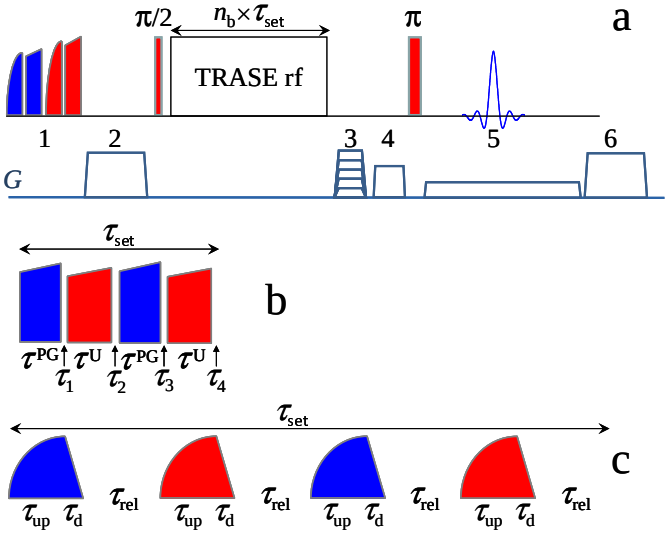

Figure 6: Main elements of the fast and slow sequences used to characterise k-space travel induced by TRASE phase-encoding. a: Main blocks for the rf current magnitude (upper line) and applied gradient (G, lower line). 1: charging pulses for the PG (blue) and U (red) coils. 2: spoiling gradient pulse. 3: optional stepped gradient pulses undoing the k-displacement of the TRASE pulse sets in a 2D sequence. 4, 5: gradient pulses for spin-echo 1D projection image of the encoded magnetisation. 6: spoiling gradient and longitudinal magnetisation recovery. The TRASE rf box consists of $n_b = 0$ to N_b chained sets of 4 rf pulses displayed in b and c for the fast and slow sequences. Elements 1 and 2 and rf blocks b were used with the fast MOSFET switches. The sequence started with the $\pi/2$ flip and used rf blocks c for the slower relay switches. All values of pulse durations and inter-pulse delays are listed in Tab. 3.

train of π-pulses applied alternatively using one of the PG coils and the U coil. For the sake of simplicity, we only used sets of 4 pulses which were repeated n_b times

(n_b ranging from 0 to N_b). The phases of the pulses with respect to a fixed carrier were

$$(\pi/2)_y^\mathrm{U} - \left[\pi_x^\mathrm{PG} - \pi_x^\mathrm{U} - \pi_{-x}^\mathrm{PG} - \pi_{-x}^\mathrm{U}\right]_{n_\mathrm{b}} - \pi_x^\mathrm{U} \qquad (6)$$

in which the superscripts refer to the coil used (colour coded in red for U and blue for PG in Fig. 6) and the subscripts y and $\pm x$ are the chosen rf phases. Each set of 4 pulses in the square brackets is expected to induce a shift in k-space $\delta\boldsymbol{k} = 4\boldsymbol{g}$ [1], and sequences in which the repeat count n_b was varied were used to sample selected k-space displacements resulting from TRASE phase-encoding in the direction of the phase-gradient vector $\boldsymbol{g}$ ($\hat{\boldsymbol{z}}$ for the $\mathrm{PG_Z}$ coil or $\hat{\boldsymbol{y}}$ for the $\mathrm{PG_Y}$ coil). This corresponds to every second step in half of the k-space of a sequential phase-encoding TRASE protocol [1].

In the absence of TRASE pulses ($n_\mathrm{b} = 0$), the echo time TE was 24 ms, with a 12-ms delay elapsed between the first (flipping) and last (refocussing) pulse written in Eq. 6. Otherwise, this delay was adjusted to still refocus the effects of the imperfect shimming of the field at time t_E, 12 ms after the refocussing π-pulse.

For the fast sequence, the energy loading scheme described in Sec. 3.3 was applied to both transmit coils used in the sequence via the relevant switches. Each repetition of the sequence started with $2\pi_x^\mathrm{PG} - 2\pi_{-x}^\mathrm{PG} - 2\pi_x^\mathrm{U} - 2\pi_{-x}^\mathrm{U}$ pairs of pulses in each coil (element 1 in Fig. 6a), followed by a spoiling gradient pulse (element 2) to remove any transverse magnetisation arising from pulse imperfections. Following the flipping $(\pi/2)_y^\mathrm{U}$ pulse, near-rectangular pulses were rapidly chained according to the pattern of Fig. 6b, with pulse durations τ^PG and τ^U and delays between pulses listed in Table 3. Pulses from the

fast		slow	
τ^PG	$6\tau_0 + \tau_0^+/2$	τ_up	$8\tau_0 + \tau_0^+$
τ^U	$6\tau_0 + \tau_0^+$	τ_d	$2\tau_0 + \tau_0^-$
τ_1	18.2 μs	τ_rel	12 τ_0
τ_2	11.6 μs	τ_set	96 τ_0
τ_3	12.2 μs		
τ_4	17.6 μs		
τ_set	32 τ_0		

Table 3: Values of pulse durations and inter-pulse delays in Figs. 6b and 6c for the fast and slow sequences, respectively. Durations are in units of the rf period τ_0 (11.95 μs) or the rounded up and down values τ_0^+ (12 μs) and τ_0^- (11.9 μs) which are multiples of the 0.1 μs base time interval of the console. The delays τ_1 to τ_4 were set to achieve the best possible start phase conditions for all the pulses while keeping the same carrier phase for simplicity. In particular, $\tau_1 + \tau_2 = \tau_3 + \tau_4 = 2\tau_0 + \tau_0^- + \tau_0^+/2$, which allows for optimal energy recovery for each tuned coil.

PG coil were set to last a half-integer number of periods ($\tau^\mathrm{PG} = 6.5\ \tau_0$) in order to avoid artefacts arising from cumulated effects of concomitant rf fields [9]. The total duration of the pattern in Fig. 6b was 32 τ_0. All switches were closed at the end of signal acquisition (element 6) to dump the rf energy before the process was restarted.

For the slower sequence, the initial energy charging and magnetisation spoiling steps were skipped, and the repeated 4-pulse pattern was that of Fig. 6c. With the relay switches, the energy storage protocol of Sec. 3.3 could not be used, and all pulses had to start and end with null current in the coil and a fully discharged tuning capacitor. Following Hoult's scheme [20] we used shaped pulses to minimise pulse durations. π-pulses consisted of a τ_up-long applied voltage to have a growing rf magnitude (as in the first part of Fig. 5d), followed by τ_d-long large inverted voltage to accelerate current magnitude decay to zero. The initial flipping $(\pi/2)_y^\mathrm{U}$ pulse had the same shape with halved amplitudes. Delays τ_rel between pulses as long as the rf pulses (12 τ_0) were sufficient for relay switching if the relay closing control signals started 4 τ_0 before the end of the previous pulse. Altogether, the total duration of the pattern in Fig. 6c was 96 τ_0, i.e. 3 times longer than for the fast sequence.

For both sequences, the elements following the TRASE rf block were identical: an optional gradient pulse in the direction of the phase-gradient vector $\boldsymbol{g}$ of the PG coil with an amplitude proportional to n_b (element 3), a standard spin-echo 1D imaging scheme (elements 4 and 5), and a final spoiling gradient pulse (element 6) with a dwell time adjusted for optimal SNR upon signal averaging of usually N_R=150 acquisitions typically lasting 250 ms each.

4.3 Results

The sequences have been run with a maximum number $N_\mathrm{b} = 24$ for the fast sequence or $N_\mathrm{b} = 8$ for the slower sequence (which correspond to the same total TRASE block duration of 768 τ_0) using three kinds of settings:

i applying both the TRASE rf pulse sets and the stepped gradient pulses (element 3 in Fig. 6a),

ii applying the TRASE rf but not the stepped gradient pulses,

iii inhibiting the TRASE rf but applying the stepped gradient pulses.

The stepped gradient pulses introduced in schemes (i) and (iii) were designed to induce k-space shifts opposite to those induced by the TRASE blocks. Figure 7 displays the spin-echo data obtained using the $\mathrm{PG_Z}$ and U coils with the fast and slow sequences, for a read gradient $G_\mathrm{r} = 0.405$ mT/m. Figures 7a and 7c compile signal magnitudes for several values of n_b. For each value, the central echo at time $t = t_\mathrm{E}$ (black trace) was obtained for setting (i), the left echo (blue trace, at $t < t_\mathrm{E}$) for setting (ii) and the right echo (red trace, at $t > t_\mathrm{E}$) for setting (iii).

Given the fair homogeneity of the static field, echo widths on the order of 70 ms FWHM were obtained for $n_\mathrm{b} = 0$ and $G_\mathrm{r} = 0$, much broader that the widths and

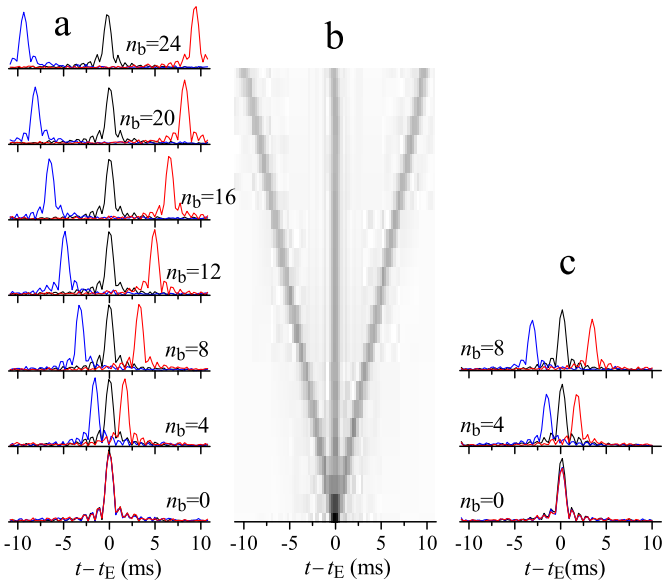

Figure 7: Spin-echo data obtained with the fast (a and b) and slow (c) sequences of Fig. 6, with the PG_Z coil and the read gradient in the z-direction. Setting (i) yields the central echoes, (ii) and (iii) yield the left and right echoes. Plot b displays the superimposed echo data of the three settings (i) to (iii) in a grayscale representation for all values of n_b from 0 (bottom) to 24 (top).

time shifts of the echoes in Fig. 7. Therefore, even a coarse adjusment of dead times before the refocussing π_x^U pulse was sufficient to avoid significant effect of stray gradients on the shape or position of the echoes in Fig. 7.

Figure 7 shows that, as expected, the gradient-only setting (iii) and the TRASE-only setting (ii) led to opposite time shifts of the echo centres increasing with the repeat count n_b, while the combined rf- and gradient-encoding in scheme (i) yielded no echo shift. The echo positions were inferred from fits of a squared sinc function to the squared echo amplitudes (the echo shapes result from 1D projection imaging of the rectangular sample). For the TRASE-only setting (ii), a linear time shift of the echo centres t_{echo} was found to be

$$t_{echo}\,(n_b) = t_E - n_b\tau_z, \text{ with } \tau_z = 0.408 \text{ ms}. \quad (7)$$

The elementary time shift τ_z corresponds to a k-space shift Δk_z per applied set of 4 rf pulses (TRASE rf block in Fig. 6b) equal to

$$\Delta k_z = 2\pi\gamma_H G_r \tau_z = 2\pi \times 7.03 \text{ m}^{-1} = 25.3°/\text{cm}, \quad (8)$$

where γ_H is the proton gyromagnetic ratio.

The stepped gradient pulses used in schemes (i) and (iii) had values $G_{step} = 76 \times n_b$ μT/m and an effective duration $\tau_{step} = 182\ \tau_0$ chosen to compensate the echo shifts induced by the applied TRASE blocks, with $G_{step}\tau_{step} = G_r\tau_z$. Apart from a small deviation from the expected positions of the echoes for $n_b = 24$ in the fast sequence (attributed to a limitation in our gradient amplifier), all data from the fast and the slow sequences consistently agree with the elementary k-space shift of Eq. 8.

The same experiments were performed using the PG_Y and U coils to quantify k-space travel in the y-direction, with values of the sequence parameters $G_r = 0.378$ mT/m, $G_{step} = 58 \times n_b$ μT/m, and $\tau_{step} = 214\ \tau_0$. Results very similar to those or Fig. 7 were obtained, and linear time shifts were inferred as in Eq. 7, with elementary time and k-space shifts amounting to

$$\tau_y = 0.38 \text{ ms} \quad (9)$$

$$\Delta k_y = 2\pi \times 6.12 \text{ m}^{-1} = 22.0°/\text{cm}. \quad (10)$$

The two k-space shifts inferred from these experiments are consistent with the values $\Delta k = 4g$ [1] where g is the computed phase-gradient vector of the relevant PG coil, but quantitatively 10% lower than expected (see Table 2).

5 Discussion

MOSFET-based switches are robust and readily available systems capable of sub-μs switching of rf power on a variety of loads. This is considerably faster than what is achieved by mechanical switches, whether magnetically actuated relays or electrostatically actuated MEMS. Moreover, mechanical switches cannot stand high applied voltages without arcing, at least during switching when the contact gap is smaller than in the open state, whereas MOSFET switches were checked to withstand high voltages even during opening and closing transients.

A general application of these features in low- and ultra-low-frequency NMR lies in shaping short rectangular pulses. When untuned transmit coils are used without switches, rectangular pulses are achieved only for a well-defined start phase and for pulses lasting an integer number of half rf periods. Failure to comply with these constraints adds transient DC components to the current in the coil at the pulse beginning and/or end (Sec. 3.2), which affect the flipping action of the pulse with flip angle and phase errors. If the pulse starts with the appropriate phase, but is interrupted after any desired duration by opening a MOSFET switch, the stored energy decays at a much higher frequency than the Larmor frequency. This transient current is much further detuned than a DC transient and therefore has a much weaker unwanted action on the magnetisation. When tuned transmit coils are used – for instance to match their impedance to low-output-impedance amplifiers – significant rise- and fall-times accompanied by phase transients affect pulse shape and pulse action on the magnetisation [8]. These limitations can be bypassed, and short, near-rectangular pulses can be repeatedly achieved in this case using an initial charging up of the tuning capacitor and subsequent use of a MOSFET switch with suitable timings to efficiently store most of that charge between pulses for times as long as hundreds of milliseconds (Sec. 3.3). Besides TRASE MRI, this energy storage approach may find applications in fast repeated spin-echo experiments.

Regarding our more specific application, MOSFET switches are efficient devices used to switch rf power between two (or more) coils to perform TRASE imaging. The ratio of impedances between the open and closed states decreases as $1/f$ because of the off-state output capacitance of the components, but is large enough for most applications up to hundreds of kHz. With their negligible switching time compared to that of electromechanical relays, they allow for a significant shortening of the time required to perform a set number of rf pulses and therefore a set displacement in k-space. In the examples of Sec. 4.3, a two-fold acceleration would result from the mere suppression of long switching times between the pulses of the slow sequences, and a three-fold acceleration is achieved if the switches are additionally used for energy storage in each of the tuning capacitors between pulses. Such acceleration could be mandatory for samples with short relaxation times or for fast-diffusing gaseous samples, for instance.

These prototype switches were quite rugged, generated negligible interference noise, and were used for an initial demonstration of k-space phase-encoding using different sets of suitable coils which met our expectations. These are suitable tools for an upcoming detailed study of TRASE operation, including for example the effects of imperfect coil decouplings through imperfectly opened switches and couplings of rf phase-gradient coils to imaging gradient coils on k-space shifts, the effects of concomitant rf fields from phase-gradient coils, and a comparison of different rf phase cycling schemes in the sequences [21].

Acknowledgements

Support from the Centre national de la recherche scientifique (CNRS) and the École normale supérieure (ENS) for joint work is gratefully acknowledged.

References

[1] J. C. Sharp, S. B. King, MRI Using Radiofrequency Magnetic Field Phase Gradients, Magnet. Reson. Med. 63 (2010) 151–161. doi:10.1002/mrm.22188.

[2] J. C. Sharp, S. B. King, Q. Deng, V. Volotovskyy, B. Tomanek, High-resolution MRI encoding using radiofrequency phase gradients, NMR Biomed. 26 (2013) 1602–1607. doi:10.1002/nbm.3023.

[3] Q. Deng, S. B. King, V. Volotovskyy, B. Tomanek, J. C. Sharp, B-1 transmit phase gradient coil for single-axis TRASE RF encoding, Magn. Reson. Imaging 31 (2013) 891–899. doi:10.1016/j.mri.2013.03.017.

[4] H. Sun, S. Yong, J. C. Sharp, The twisted solenoid RF phase gradient transmit coil for TRASE imaging, J. Magn. Reson. 299 (2019) 135–150. doi:10.1016/j.jmr.2018.12.015.

[5] E. Der, V. Volotovskyy, H. Sun, B. Tomanek, J. C. Sharp, Design of a high power PIN-diode controlled switchable RF transmit array for TRASE RF imaging, Concepts Mag. Reson. B 48 (2018) e21365. doi:10.1002/cmr.b.21365.

[6] S. Kumaragamage, M. Lang, D. Ostapchuk, C. Bidinosti, B1 phase gradient coil design for low field exploration of TRASE MRI, in: Proc. ESMRMB 33, Magn. Reson. Mater. Phy. 29 (Suppl 1), 2016, p. S34.

[7] C. Bidinosti, P.-J. Nacher, G. Tastevin, Concomitant B1 Field in Low-Field MRI: Potential Contributions to TRASE Image Artefacts, in: Proc. Intl. Soc. Mag. Reson. Med. 26, 2018, p. 2670.

[8] C. Bidinosti, P.-J. Nacher, G. Tastevin, Unconventional trajectories on the Bloch Sphere: A closer look at the effects and consequences of the breakdown of the rotating wave approximation, in: Proc. Intl. Soc. Mag. Reson. Med. 26, 2018, p. 2701.

[9] P.-J. Nacher, G. Tastevin, C. Bidinosti, Exploration of TRASE MRI at Low Magnetic Field: Potential Performance and Limitations, in: Proc. 14 th Euromar, 2018, p. P338.

[10] P. Horowitz, W. Hill, The Art of Electronics, 3rd Edition, Cambridge University Press, New York, NY, USA, 2015, Chapter 3.5 (Ch. 3.14 in 2nd Edition).

[11] S. Mandal, S. Utsuzawa, D. G. Cory, M. Huerlimann, M. Poitzsch, Y. Q. Song, An ultra-broadband low-frequency magnetic resonance system, J. Magn. Reson. 242 (2014) 113–125. doi:10.1016/j.jmr.2014.02.019.

[12] J. Zhen, K. O'Neill, E. Fridjonsson, P. Stanwix, M. Johns, A resistive Q-switch for low-field NMR systems, J. Magn. Reson. 287 (2018) 33–40. doi:10.1016/j.jmr.2017.12.006.

[13] P.-J. Nacher, S. Kumaragamage, G. Tastevin, C. Bidinosti, A Fast MOSFET Switch for RF Pulse Management and Shaping in Low-Field NMR and MRI, in: Proc. 14 th Euromar, 2018, p. O44.

[14] C. Bidinosti, I. Kravchuk, M. Hayden, Active shielding of cylindrical saddle-shaped coils: Application to wire-wound RF coils for very low field NMR and MRI, J. Magn. Reson. 177 (2005) 31–43. doi:10.1016/j.jmr.2005.07.003.

[15] C. Bidinosti, C.-Y. Liu, S. King, The intrinsic magnetic field symmetries of the spiral birdcage coil, in: Proc. Intl. Soc. Mag. Reson. Med. 18, 2010, p. 1509.

[16] J. Bellec, C.-Y. Liu, S. King, C. Bidinosti, A Target Field Approach to the Design of RF Phase-Gradient Coils, in: Proc. Intl. Soc. Mag. Reson. Med. 19, 2011, p. 723.

[17] K. Safiullin, C. Talbot, P.-J. Nacher, Achieving high spatial resolution and high SNR in low-field MRI of hyperpolarised gases with Slow Low Angle SHot, J. Magn. Reson. 227 (2013) 72–86. doi:10.1016/j.jmr.2012.11.025.

[18] C. P. Bidinosti, J. Choukeife, P.-J. Nacher, G. Tastevin, In vivo NMR of hyperpolarized 3He in the human lung at very low magnetic fields, J. Magn. Reson. 162 (2003) 122–132. doi:10.1016/S1090-7807(02)00198-2.

[19] V. V. Kuzmin, P.-J. Nacher, Signal feedback applications in low-field NMR and MRI, J. Magn. Reson. (2019) 106622doi:10.1016/j.jmr.2019.106622.

[20] D. I. Hoult, Fast Recovery, High Sensitivity NMR Probe and Pre-Amplifier for Low-Frequencies, Rev. Sci. Instrum. 50 (1979) 193–200. doi:10.1063/1.1135786.

[21] P. Bohidar, H. Sun, G. E. Sarty, J. C. Sharp, TRASE 1D sequence performance in imperfect B1 fields, J. Magn. Reson. 305 (2019) 77–88. doi:10.1016/j.jmr.2019.06.005.